# High-throughput screening of the thermoelastic properties of ultra-high temperature ceramics

Pinku Nath,[1] Jose J. Plata,[2] Julia Santana,[2] Ernesto J. Blancas,[2] Antonio M. Márquez,[2] and Javier Fdez. Sanz[2]

[1] *Lovely Professional University, India*

[2] *Departamento de Química Física, Universidad de Sevilla, Seville, Spain**

(Dated: January 20, 2022)

Ultra-high temperature ceramics, UHTCs, are a group of materials with high technological interest because their use in extreme environments. However, their characterization at high temperatures represents the main obstacle for their fast development. Obstacles are found from a experimental point of view, where only few laboratories around the world have the resources to test these materials under extreme conditions, and also from a theoretical point of view, where actual methods are extremely expensive. Here, a new theoretical high-throughput framework for the prediction of the thermoelastic properties of materials is introduced. This approach can be systematically applied to any kind of crystalline material, drastically reducing the computational cost of previous methodologies. Elastic constants for UHTCs have been calculated at a wide range of temperatures with excellent agreement with experimentally reported values. Moreover, other mechanical properties such a bulk modulus, shear modulus or Poisson ration have been also explored. Other frameworks with similar computational cost have been used only for predicting isotropic or averaged properties, however this new approach opens the door to the calculation of anisotropic properties at a very low computational cost.



## I. INTRODUCTION

Ultra-high temperature ceramics, UHTCs, are usually defined as compounds whose melting point surpasses 3000°C [1–3]. While UHTCs are not new materials for the scientific community and have been reported since late 1800s [4, 5], their technological interest started to grow in the late 1960s [6]. In the most recent decade, UHTCs have clearly emerged because of their potential use in extreme environments [2]. Aerospace applications such as scramjet propulsion, hypersonic aerospace vehicles and advanced rocket motors are the main reason why research on UHTCs has grown in recent years [7]. For instance, thermal control, mechanical resistance and corrosion are the main variables to consider when designing hypersonic vehicles, whose materials experience temperatures higher than 2000°C and are exposed to highly-reactive, dissociated gas species [8]. UTHCs combine high hardness, stiffness, and melting temperature with very low reactivity because of their strong covalent bonds between carbon, nitrogen or boron with transition metals, TM, such as Hf, Zr, Nb, Ti or Ta [9, 10].

UHTCs-based materials have been rapidly developed during the last 25 years [11–14], but there are still many challenges to be tackled in order to spur the rational design, synthesis and deployment of these materials. The main issue that hampers the swift development of these materials is their experimental characterization and testing at extreme environments. Most well-known properties of these materials are obtained at ambient conditions and there are few laboratories around the world with the resources to test materials under extreme conditions [15–19]. Thus far, computational approaches have not presented solutions to these experimental barriers. Most of theoretical works related to UHTCs are focused on 0 K properties [20–22] and there are few reports in which temperature-dependent mechanical properties of UHTCs are explored [23, 24]. This has been due to i) the lack of commercial algorithms to predict these temperature-dependent properties and ii) the high computational cost of these calculations.

There are methods, such as the quasi-harmonic approximation, QHA [25–27], that provide a relatively inexpensive computational approach to obtain temperature-dependent mechanical properties such as bulk or shear modulus. However, QHA is most frequently used with isotropic volume deformations of the crystal, so the properties obtained through this method can be considered as average mechanical features of the system. That is the reason why elastic constants need to be computed in order to fairly capture the anisotropy of the material and obtain a more complete description of the temperature-dependent mechanical response of the system [28, 29]. Thus, elastic constants represent the starting point that gives access to other mechanical properties. Different approaches have been proposed to compute temperature-dependent elastic constants using QHA as a formal framework [30–33]. However, their computational costs prevent them from being used systematically or routinely. Other methods have been developed in order to reduce the cost of using the QHA to compute temperature-dependent elastic constants [34–37]. For instance, the quasi-static approximation, QSA, reduces the number of calculations, assuming that the temperature dependence of the elastic constant is primarily due to thermal expansion [34, 35]. Nevertheless, QSA tends to underestimate thermal effects and increase anisotropy, which is in detrimental to its use, especially at high temperatures [38].

In this work, the elastic constants of UHTCs at finite temperatures are predicted to chart their mechanical properties, paying special attention to the high temperature range, in order to simulate their behavior at extreme conditions. To do so, a new high-throughput framework has been designed that not only automatises the process, but also includes a new approach that reduces the computational cost compared with previous methodologies, without

* jplata@us.es

losing accuracy.

## II. METHODOLOGY

### A. Elastic constants

Traditionally, elastic properties can be described within the Lagrangian theory of elasticity in which a solid is considered as a homogeneous and anisotropic elastic medium [39]. Within a linear regime and using the Voigt notation, the stress, $\boldsymbol{\sigma}$=$(\sigma_1, \sigma_3, \sigma_3, \sigma_4, \sigma_5, \sigma_6)$, and strain, $\boldsymbol{\epsilon}$=$(\epsilon_1, \epsilon_2, \epsilon_2, \epsilon_2, \epsilon_2, \epsilon_6)$, relation can be expressed as [38, 40, 41]

$$\sigma_i = \sum_{j=1}^{6} c_{ij}\epsilon_j, \tag{1}$$

where $c_{ij}$ are elastic stiffness constants of a crystal represented in a $6 \times 6$ matrix where $c_{ij} = c_{ji}$. Considering this constraint, the total number of independent elastic components are 21 instead of 36. Alternatively, it is possible to define the total energy of a crystal in terms of a power series of the strain [28] as

$$E(\boldsymbol{\epsilon}) = E_0 + V_0 \sum_i \sigma_i^{(0)}\epsilon_i + \frac{V_0}{2!}\sum_{i,j} c_{ij}\epsilon_i\epsilon_j + ... \tag{2}$$

where $E_0$ and $V_0$ are the DFT energy and volume of the reference structure. If the optimized (ground state) structure is chosen as the reference, $\sigma_i^{(0)} = 0$ because equilibrium structure is stress free.

Two alternative expressions can be derived for the elastic constants according to Eqs. 1 and 2,

$$c_{ij} = \left.\frac{\partial \sigma_i}{\partial \epsilon_j}\right|_{\boldsymbol{\epsilon}=0} \tag{3}$$

and

$$c_{ij} = \left.\frac{1}{V_0}\frac{\partial^2 E}{\partial \epsilon_i \partial \epsilon_j}\right|_{\boldsymbol{\epsilon}=0}. \tag{4}$$

Methods based on Eq. 3 to calculate $c_{ij}$ are defined as "stress approach", while methods based on Eq. 4 are classified as "energy approach". Although both are based on the creation of strained structures, there are important differences between them. The stress-strain approach is the most used method and a lower number of strained structures are needed [42, 43]. However, time-consuming calculations are required to obtain the same accuracy as with the results obtained with the energy-strain method using a less demanding setup [29]. That is why the energy-strain method is preferred to reduce the sensitivity of the results with respect to the calculation setup. When the energy-strain method is used, a set of distortion or deformation modes are chosen depending on the crystal symmetry [28]. For each distortion mode, different structures are created in which the amplitude or magnitude of the deformation is modified obtaining energy-strain curves. Elastic constants at 0 K can be calculated using these curves.

### B. Free energy and the quasiharmonic approximation

In QHA, the total free energy, $F$, of a system is a function of volume, $V$, and temperature, $T$, and it is described as the sum of three terms (Eq. 5): i) the vibration less total energy at 0 K, $E_0$, ii) the vibrational free energy, $F_{\text{vib}}$ and iii) free energy due to thermal electronic excitations, $F_{\text{elec}}$ [44–46]. The first term of the equation can be computed with different *ab-initio* packages [47, 48]. The second term is obtained integrating over the phonon density of states, pDOS [27, 49, 50]. The last term of the equation is calculated integrating over the electronic density of states, DOS.

$$F(V,T) = E_0(V) + F_{\text{vib}}(V,T) + F_{\text{elec}}(V,T). \tag{5}$$

The calculation of $F_{\text{vib}}$ at a given $V$ is performed using the harmonic approximation, where $F_{\text{vib}}$ includes anharmonic effects in the form of volume-dependent phonon frequencies [27, 44–46, 49],

$$F_{\text{vib}}(V,T) = \frac{1}{N_q}\sum_{\mathbf{q},j}\left(\frac{\hbar\omega_j(\mathbf{q})}{2} + k_{\text{B}}T\ln\left[1-\exp\left(-\frac{\hbar\omega_j(\mathbf{q})}{k_{\text{B}}T}\right)\right]\right), \tag{6}$$

where $\hbar$ and $k_{\text{B}}$ are the reduced Planck and Boltzmann constants, and $\omega_j(\mathbf{q})$ is the volume-dependent phonon frequency for the wave vector, $\mathbf{q}$, and phonon branch index $j$. $N_q$ is the total number of wave vectors.

For metals and narrow band-gap systems, the contribution of $F_{\text{elec}}(V,T)$ to $F$ could be important and includes temperature-dependent contribution of the electrons to the internal energy, $U_{\text{elec}}(V,T)$, and the electronic entropy,

$S_{\text{elec}}(V,T)$ [44, 45, 49, 51]:

$$F_{\text{elec}}(V,T) = U_{\text{elec}}(V,T) - TS_{\text{elec}}(V,T). \quad (7)$$

Both terms can be calculted as,

$$U_{\text{elec}}(V,T) = \int_0^{\infty} n_{\text{elec}}(\epsilon) f(\epsilon) \epsilon d\epsilon - \int_0^{E_F} n_{\text{elec}}(\epsilon) \epsilon d\epsilon \quad (8)$$

and

$$\begin{aligned} S_{\text{elec}}(V,T) = &- k_B \int_0^{\infty} n_{\text{elec}}(\epsilon) [f(\epsilon) \ln(f(\epsilon)) + \\ &+ (1 - f(\epsilon)) \ln(1 - f(\epsilon))] d\epsilon \end{aligned} \quad (9)$$

where $n_{\text{elec}}(\epsilon)$ is the density of states at energy $\epsilon$, $f(\epsilon)$ is the Fermi-Dirac distribution, and $E_F$ is the Fermi energy.

The temperature-dependent isothermal elastic constants, $c_{ij}^T(T)$, can be obtained by minimizing temperature dependent free energy, $F(\boldsymbol{\epsilon},T)$ with respect to strain by using similar methodology as shown in Eq. 4. The strain dependent $F(\boldsymbol{\epsilon},T)$ at a given temperature, $T$ is defined as:

$$F(\boldsymbol{\epsilon},T) = E_0(\boldsymbol{\epsilon}) + F_{\text{vib}}(\boldsymbol{\epsilon},T) + F_{\text{elec}}(\boldsymbol{\epsilon},T), \quad (10)$$

where $F_{\text{vib}}$ and $F_{\text{elec}}$ represent the vibrational and thermal electronic excitations of free energies. It is important to notice that $F_{\text{vib}}(\boldsymbol{\epsilon},T)$ and $F_{\text{vib}}(V,T)$ are equivalent terms, because any strain applied to the material is directly connected to a specific volume.

### C. Accelerated QHA (QHA3P)

The $F_{\text{vib}}$ in Eq. 5 is a function of $V$ and requires lattice dynamic calculations at several volumes. This approach consumes large computational resources but it can be avoided with the use of the QHA3P method [49]. In the QHA3P method, three phonon calculations are performed at three different volumes, one at the DFT optimized volume, $V_0$, and the other two at $V_0 \pm \Delta V$ volumes. $\Delta V$ represents small distorted volume from $V_0$. The three obtained phonon frequencies are then used to extrapolate to any given volume at a given $\mathbf{q}$ using [49, 52]:

$$\begin{aligned} \omega(\mathbf{q},V) = &\omega(\mathbf{q},V_0) + \left(\frac{\partial\omega(\mathbf{q})}{\partial V}\right)_{V_0} (\Delta V) \\ &+ \frac{1}{2}\left(\frac{\partial^2\omega(\mathbf{q})}{\partial V^2}\right)_{V_0} (\Delta V)^2, \end{aligned} \quad (11)$$

The remaining steps to compute thermodynamic properties are the same as in the QHA.

### D. Isothemal and adiabatic elastic constants

As mentioned previously, isothermal elastic stiffness constants, $c_{ij}^T(T)$, can be calculated at finite temperatures by substituting internal Energy, $E$, by free energy, $F$, in Eq. 4,. However, from an experimental point of view, elastic constants are generally obtained in adiabatic rather than isothermal conditions, using techniques such as ultrasonic measurements or Brilluoin scattering experiments [53, 54]. Adiabatic elastic constants, $c_{ij}^S(T)$, are always equal to or larger than $c_{ij}^T(T)$. In order to compare with experiments, $c_{ij}^T(T)$ are converted into $c_{ij}^S(T)$ following the relation reported by Davies[30],

$$c_{ij}^S = c_{ij}^T + \frac{TV}{C_V}\lambda_i\lambda_j, \quad (12)$$

where

$$\lambda_i = \sum_k \alpha_k c_{ik}^T, \quad (13)$$

$\alpha_i$ is the linear thermal expansion coefficient in the direction $i$, $C_V$ is the specific heat and $\rho$ is the density. For cubic systems [38]:

$$\lambda_1 = \lambda_2 = \alpha\left(c_{11}^T + c_{12}^T\right) \quad (14)$$

and $\lambda_4 = 0$ so $c_{44}^S = c_{44}^T$. For hexagonal systems [55],

$$\lambda_1 = \lambda_2 = \alpha_a\left(c_{11}^T + c_{12}^T\right) + \alpha_c c_{13}^T \quad (15)$$

and

$$\lambda_3 = 2\alpha_a c_{13}^T + \alpha_c c_{33}^T, \quad (16)$$

where $\alpha_a$ and $\alpha_c$ are he linear expansion coefficients in the directions "$a$" and "$c$".

### E. Workflow and computational details

A high-throughput framework has been developed to automate the calculation of the temperature-dependent mechanical properties of UHTCs (Fig. 1). First, the primitive cell is fully optimized to characterize the minimum of the potential surface energy at 0 K. The energy-strain method is used to calculate the elastic constants of each material so their space groups are calculated using spglib library [56] to identify the inequivalent $c_{ij}$. Thirteen volume-distorted cells are generated for each inequivalent $c_{ij}$, 6 of them with a negative strain and 6 of them with a positive strain. The set of distortion modes have been chosen following Zhang *et al.* approach [40]. For instance, the distortions for cubic system are $\boldsymbol{\epsilon}_1 = (0,0,0,\delta,\delta,\delta)$, $\boldsymbol{\epsilon}_2 = (\delta,\delta,0,0,0,0)$ and $\boldsymbol{\epsilon}_3 = (\delta,\delta,\delta,0,0,0)$. Where $\delta$ represents the magnitude of strain and goes from -2% to +2% of each lattice vector to obtain the 13 volume-distorted cells for each $\boldsymbol{\epsilon}_i$. In order to compute $F(\boldsymbol{\epsilon},T)$, only three phonon calculations, including two distortions, $\delta$, and the fully-optimized geometry are required for a given $\boldsymbol{\epsilon}$. The frequencies obtained for these three structures are then used to estimate other frequencies for any arbitrary $\delta$ values for that particular $\boldsymbol{\epsilon}_i$ using a Taylor expansion. Thus, for a cubic system a total of seven phonon calculations are required, including

one phonon calculation at $\boldsymbol{\epsilon} = 0$ state. This approach is much less computationally demanding than QHA where, approximately, 37 phonon calculations are required (13 $\delta$ per $\boldsymbol{\epsilon}_i$). Finally, $F(\boldsymbol{\epsilon}, T)$ are fitted with cubic polynomial to extract elastic constants [38].

**Geometry optimization.** All 0 K ground state structures were fully relaxed (atoms and lattice) using VASP package [47, 57]. Energies were obtained combining the projector-augmented wave (PAW) potentials [58] with the exchange-correlation functional proposed by Perdew-Burke-Ernzerhof (PBE) [59]. The number of valence electrons for each atom was selected following standards proposed by Calderon *et al.* [60]. All calculations use a high-energy cut-off, 700 eV for borides and 550 eV for carbides and nitrides. Reciprocal space was explored using a dense **k**-point mesh of 12,000 **k**-points per reciprocal atom, approximately. Wavefunction was converged self-consistently until the energy difference between two consecutive electronic steps was smaller than $10^{-9}$ eV. Partial occupancies for each orbital were determined using Methfessel-Paxton method of order one. Geometry optimizations were performed using three-atom primitive cell for borides and 8-atoms conventional cells for carbides and nitrides. Structures were considered fully relaxed when forces over all atoms were smaller than $10^{-8}$ eV/Å. An additional support grid for the evaluation of the augmentation charges was included to reduce the noise in the forces.

**Distorted cells.** Elastic constants prediction requires three and five distortion modes for cubic and hexagonal systems, respectively. These distortion modes are generated using the procedure shown in Ref. [40]. Thirteen values of $\delta$ have been chosen within the range $\pm$ 2% for a $\boldsymbol{\epsilon}_i$. These generated structures are relaxed without changing the cell volume. After the relaxation, single point calculations were performed for each volume-distorted cell in order to calculate their density-of-states, DOS.

**Phonon calculations.** Different packages can be used to predict the vibrational spectra of solids, such as Alamode [61], APL-AAPL [62], PHON [63] or Phonopy [50]. In this case, phonon calculations were performed combining Phonopy and VASP to obtain second-order interatomic force constants, IFCs, via the finite displacement approach [27]. For each $\boldsymbol{\epsilon}_i$, two phonon calculations are performed at $\pm$2% distortions including one at equilibrium structure. Forces were extracted from $4 \times 4 \times 4$ supercells for borides (192 atoms) and $3 \times 3 \times 3$ supercells for nitrides and carbides (216 atoms). The magnitude of the displacement to obtain the force constants was 0.01 Å. The same SCF convergence criteria followed in the optimizations was used for these calculations. Frequencies and other related phonon properties such as $F_{\text{vib}}$ were calculated using a $31 \times 31 \times 31$ **q**-point mesh that ensures their convergence.

## III. RESULTS

### A. Phonon dispersion curves

Phonon dispersion curves are an essential part to compute the vibrational contribution to the free energy and, simultaneously, give information about the stability of these materials. The absence of imaginary frequencies confirms the dynamic stability of UHTCs at 0 K (Fig. S1). Moreover, our results are in good agreement with previous theoretical predictions [64], and, most importantly, experimental data [65–72]. Only small deviations were found for the borides, which can be attributed to the measurement of the phonon dispersion curve at finite temperatures and specific surfaces [65].

### B. Elastic constants

In this section, calculated isothermal and isentropic elastic constants are compared with previous experimental values and simulations where available (Fig. 2). To the best of our knowledge, $TiB_2$ and $ZrB_2$ are the only two UHTCs whose elastic constants have been experimentally well characterized in a wide range of temperatures [73, 74]. The values obtained with the new high-throughput framework are in excellent agreement with the experiments and other calculated values obtained with more computationally demanding approaches [24, 75] (Fig. S2). Experimental results, but in a shorter range of temperatures, were also found for TiC and ZrC [76], with relative errors always below 5%. Only room temperature values have been reported for ZrN and HfN [77], so it is difficult to analyze any trends. That is why, we have also included calculated 0 K elastic constants for these two systems [78]. In both materials, calculated and experimental available results are aligned with our results and only $c_{11}$ at 300 K present a small deviation. Only calculated values have been found for TiN [79] and HfC [80]. Molecular dynamics performed by Steneteg *et al.* seem to predict similar trends and values than the HT framework for TiN. For HfC, Zhang *et al.* obtained very similar values for $c_{12}$ and $c_{44}$ while $c_{11}$ seems to decrease faster than in our results. However, they also obtained a very soft behavior of $c_{11}$ for ZrC [80], while our methodology seems to follow the experimental measurements better. The fast reduction of $c_{11}$ with temperature is more noticeable for nitrides. This trend is related to the changes in the volume when longitudinal strains are applied, which is strongly connected to temperature. Other elastic constants such as $c_{12}$ and $c_{44}$ are related to deformation resistance to strain modes that are not connected to big changes in the volume, so they are less affected by temperature.

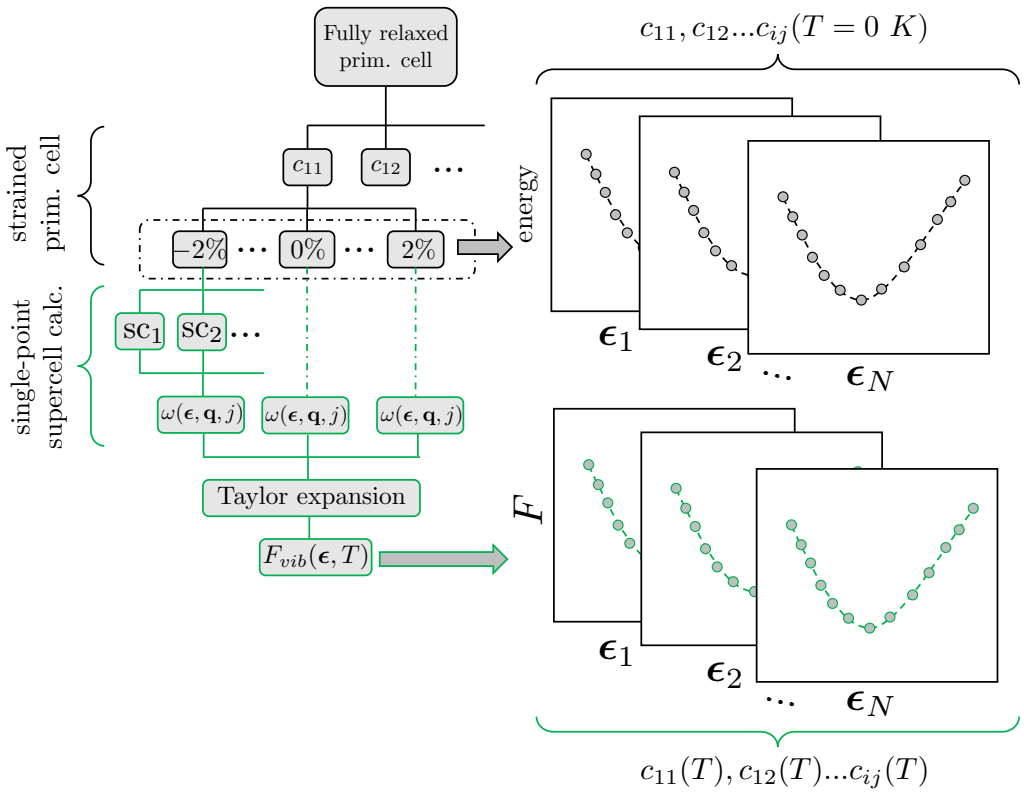


FIG. 1. The workflows for calculating temperature dependent elastic constants.

### C. Mechanical stability

Elastic constants describe the response of the crystal to external forces, so they play an important role determining their mechanical stability. Mechanical stability has been extensively explored by different theoretical and computational works [81]. Here, Born stability criteria [82] will be adopted to elucidate the mechanical stability of these materials in a wide range of temperatures. For a cubic crystal, the mechanical stability criteria [83] under isotropic pressure are,

$$\begin{aligned} &c_{44} > 0, \\ &c_{11} - c_{12} > 0, \\ &c_{11} + 2c_{12} > 0. \end{aligned} \tag{17}$$

For hexagonal systems, the stability criteria [84, 85] are:

$$\begin{aligned} &c_{44} > 0, \\ &c_{11} - c_{12} > 0, \\ &(c_{11} + c_{12})\, c_{33} - 2c_{13}^2 > 0. \end{aligned} \tag{18}$$

All the materials explored in this work fulfil the Born stability criteria in the studied range of temperatures (Fig. S3).

### D. Isotropic mechanical properties

Elastic constants are the essential ingredient to compute some key isotropic mechanical properties such as bulk modulus, $B$, shear modulus, $G$, Young's modulus $Y$, poisson ratio $\sigma$ and hardness $H_{\mathrm{V}}$.

**Bulk modulus and Shear.** Different definitions have been proposed to calculate the bulk modulus of an aggregate of crystals. Voigt´s definition is based on the averaging of the relation expressing the stress in a single crystal over all possible orientations [86],

$$9B_{\mathrm{V}}^{X} = \left(c_{11}^{X} + c_{22}^{X} + c_{33}^{X}\right) + 2\left(c_{12}^{X} + c_{23}^{X} + c_{31}^{X}\right), \tag{19}$$

where $X = (S, T)$ in order to differentiate between adiabatic and isothermal values, respectively. While Voigt´s definition assumes that the strain is uniform through the aggregate, Reuss´ approach consider that the stress is uniform [87],

$$\frac{1}{B_{\mathrm{R}}^{X}} = \left(s_{11}^{X} + s_{22}^{X} + s_{33}^{X}\right) + 2\left(s_{12}^{X} + s_{23}^{X} + s_{31}^{X}\right), \tag{20}$$

where $\boldsymbol{s}^{X}$ is the compliance tensor,

$$\boldsymbol{s} = \boldsymbol{c}^{-1}. \tag{21}$$

It has been proven that Voigt moduli are always larger that Reus moduli with true values lying between them [88]. That is why, the Voigt-Reuss-Hill bulk modulus, $B_{\mathrm{VRH}}^{X}$, is defined as,

$$B_{\mathrm{VRH}}^{X} = \frac{1}{2}\left(B_{\mathrm{V}}^{X} + B_{\mathrm{R}}^{X}\right). \tag{22}$$

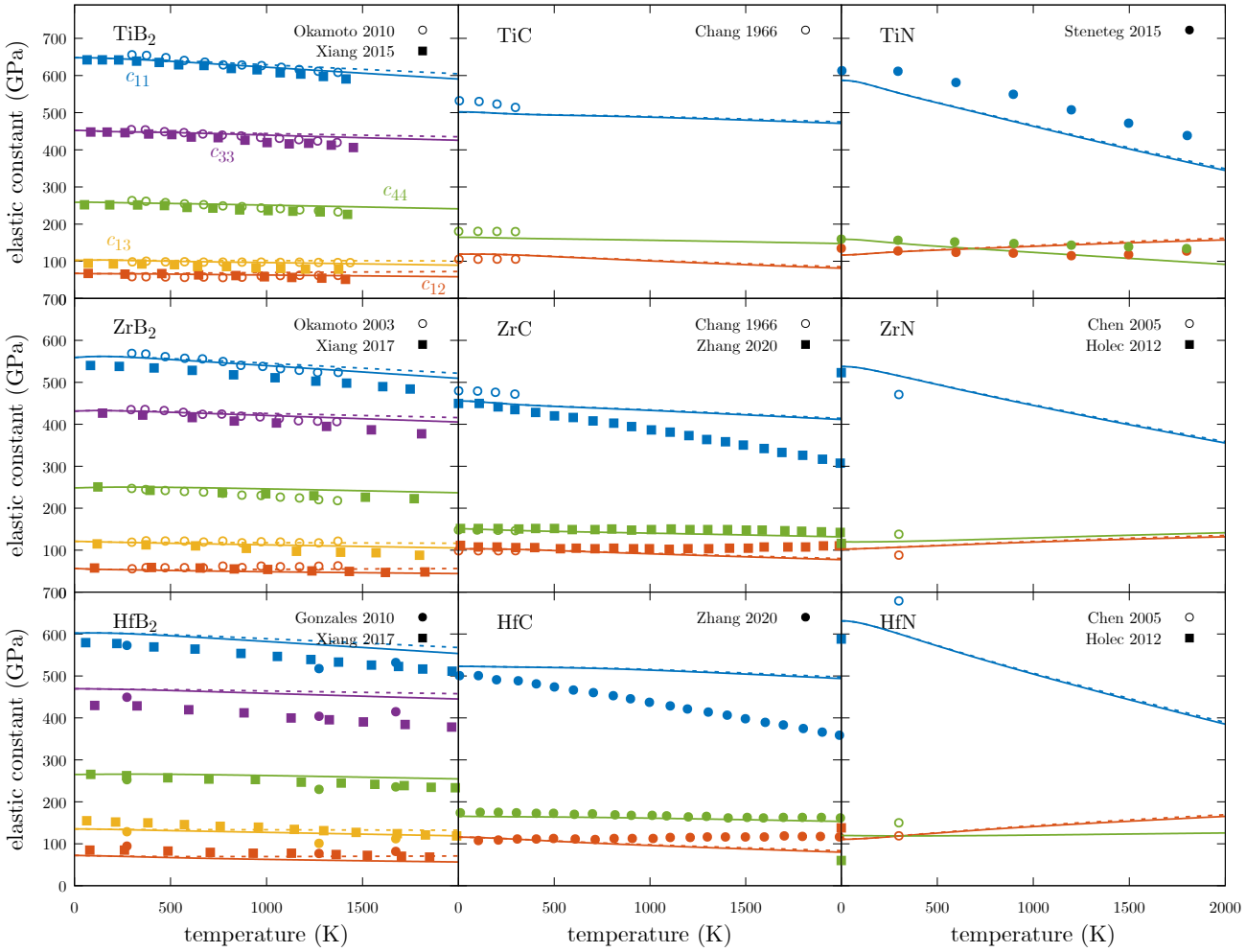


FIG. 2. Isothermal (solid lines) and isentropic (dashed lines) elastic constants for UHTCs. Open points represent experimental measurements while filled points represent calculated values. Colors: $c_{11}$ = blue; $c_{12}$ = orange; $c_{13}$ = yellow; $c_{33}$ = purple; $c_{44}$ = green.

Similarly, Shear modulus can be defined as,

$$G_{\mathrm{V}}^{X} = \frac{1}{15}\left(c_{11}^{X}+c_{22}^{X}+c_{33}^{X}\right)-\left(c_{12}^{X}+c_{23}^{X}+c_{31}^{X}\right)+ \\ +3\left(c_{44}^{X}+c_{55}^{X}+c_{66}^{X}\right) \tag{23}$$

or

$$15/G_{\mathrm{R}}^{X} = 4\left(s_{11}^{X}+s_{22}^{X}+s_{33}^{X}\right)-4\left(s_{12}^{X}+s_{23}^{X}+s_{31}^{X}\right)+ \\ +3\left(s_{44}^{X}+s_{55}^{X}+s_{66}^{X}\right). \tag{24}$$

Again, $G_{\mathrm{R}}^{X} < G_{\mathrm{V}}^{X}$ and real values should lie in between so,

$$G_{\mathrm{VRH}}^{X} = \frac{1}{2}\left(G_{\mathrm{V}}^{X}+G_{\mathrm{R}}^{X}\right). \tag{25}$$

Taking into account the small difference between isentropic and isothermal elastic constants and, in order to simplify the analysis of the results, $B^T$ and $G^T$ will be used to compute the other properties presented in this work.

The comparison of simulations with experimental values for $B$ and $G$ is not a simple task (see Fig. 3). Most of the time, experimental measurements are obtained from polycrystalline samples in which porosity plays an important role, modifying their mechanical properties. There are different models that correlate the mechanical properties of the fully dense material and the porosity with the mechanical properties of actual sample [89–91]. Here, the Gibson and Ashby equation [92] was adopted to compare the experimental $B$, $G$ and Young's modulus, $Y$, with the theoretical results, if the porosity of the sample was reported. For instance, predicted values are in excellent agreement with experimental measurements [93, 94] for the $B$ and $G$ of borides, once porosity is considered. A similar trend is also found for TiC where experimental values are also available [76, 95]. Larger deviations with respect to experimental values are obtained for HfN where $G$ is underestimated around 15% at 298 K. Comparing with other previous theoretical results also helps to demonstrate how this new approach can be not only accurate but also how it can substantially reduce the computational time. For instance, the values obtained for $B$ and $G$ match well

with the results reported by methods based on the QHA in which phonon calculations are performed for all distorted structures for ZrC and HfC [80], TiN [96, 97] and ZrN [98].

**Young's modulus and Poisson ratio.** Young's modulus, $Y$, is a directional property, however, it can be initially assumed isotropic in order to extract a single approximate value for each compound,

$$Y = 2G(1+\sigma), \tag{26}$$

where $\sigma$ is the isotropic Poisson ratio,

$$\sigma = \frac{(3B-2G)}{(6B+2G)}. \tag{27}$$

Similarly to $B$ and $G$, our calculations are in good agreement with experimental values, when available for $Y$ (Fig. 3). Calculated values for borides [93, 94] present a maximum relative error around 7% at high temperatures, which is very small considering: i) the values are obtained using a very simple model to take into account the porosity of the sample [99, 100] and ii) high-order force constants, which are not calculated here, can play an important role at high temperatures. Similar trends are observed for TiC [76, 95] and ZrC [101, 102], where predicted $Y$ values are slightly underestimated, but follow the same trend as experimental measurements. If experimental reports were not available, previous theoretical works were used to evaluate the results obtained with this new high-throughput approach. No significant discrepancies were found when $Y$ values were compared with the results obtained with methods based on the QHA (see ZrC and HfC [80]). Larger differences were found for TiN where Steneteg *et al.* used molecular dynamics to study the mechanical properties of TiN [79]. However, $Y$ experimental values for TiN single crystals at room temperature are between 445-449 GPa [103], which are close to the values calculated in this work.

To the best of our knowledge, there are not many experimental studies of the temperature dependence of the Poisson ratio. For instance, Wiley *et al.* explored the Poisson ratio of the borides of the group IV up to 1300 K [93]. Our results are not only in agreement at room temperature, but also reproduce the very small variation that this property presents in a large temperature range (Table I). When compared with borides, the temperature dependence is slightly higher for carbides but is even larger in TiN and HfN. This trend is also observed in the wider range of experimental values previously reported (Table I).

**Hardness.** Hardness is probably one of the most difficult mechanical properties to predict and compare with experimental data. It not only presents a dependency with the porosity [106] or grain size [107], but also with other variables related to the measurement, such as indentation type (nano or micro), load and time [108, 109]. During the last two decades, different models have been proposed to predict the hardness of materials [110–112]. Most of them assume isotropic conditions which could overestimate the hardness of some materials, depending on the crystal plane exposed on the surface. [113]. Moreover, porosity and indentation load tend to reduce the values obtained for hardness [100]. Here, hardness is calculated using the approach proposed by Tian *et al.* [114],

$$H_{\mathrm{V}} = 0.92k^{1.137}G^{0.708}, \tag{28}$$

where $k$ is the Pugh's modulus, which is defined as the ratio between the shear, $G$, and the bulk modulus, $B$. In Eq. 28, the constants are adjusted to obtain $H_{\mathrm{V}}$ in GPa units. At room temperature, borides seem to be the most overstimated values obtaining 47 GPa, 41 GPa and 42 GPa for $TiB_2$, $ZrB_2$ and $HfB_2$ when experimental values range between 34-22 GPa [100, 115–117], 39-20 GPa [118–120] and 33-31.4 GPa [121, 122], respectively (Fig. 4). TiC stands as a good example of the different values that can be obtained for hardness, depending on the plane and orientation of the crystal [105, 123, 124]. For instance, TiC (100) plane on the [110] direction presents a micro-Vickers hardness of 34.9 GPa while the values for the (110) plane at the [100] direction is 23.24 GPa [123]. Using the approach proposed by Tian, the calculated value (24.1 GPa) is in that range experimentally reported at room temperature. Similarly, calculated hardness for ZrC (23.2 GPa) and HfC (25.2 GPa) are in good agreement with the experimental measurements [125–129]. To the best of our knowledge, there are not too many experimental works which study the hardness of nitrides, however we have found that calculated values are slightly lower than the homolog carbides and are close to the reported values for TiN [130], ZrN [131] and HfN [77].

If predicting hardness is a difficult task because of the wide range of experimental variables, capturing the temperature dependence of this property is even more of a challenge. Hardness changes with temperature. Especially at high temperatures, hardness is controlled by creep due to dislocation diffusion phenomena. The activation energy for creep can be calculated from

$$H_{\mathrm{V}}^{-m} = A\exp(-Q/RT)t \tag{29}$$

where $Q$, $R$, $T$, and $t$ are the activation energy for creep, the gas constant, the temperature and loading time, respectively, and m and A are constants [132, 133]. When Arrhenius plots are used to study hardness in a temperature range, different regions are identified for many UHTCs [116, 119, 123, 125, 134]. These regions are linked to a brittle-ductile transition and the different mechanisms that govern the deformation during the indentation at different temperatures [125]. Activation energies for creep for borides and carbides have been reported to be around 80 kcal/mol and most of experimental studies obtain values for $m$ between 4 and 5 [123, 125]. These values can be combined with our predictions at room temperature to calculate the pre-exponential constant and obtain good trends for hardness below 1000 K.

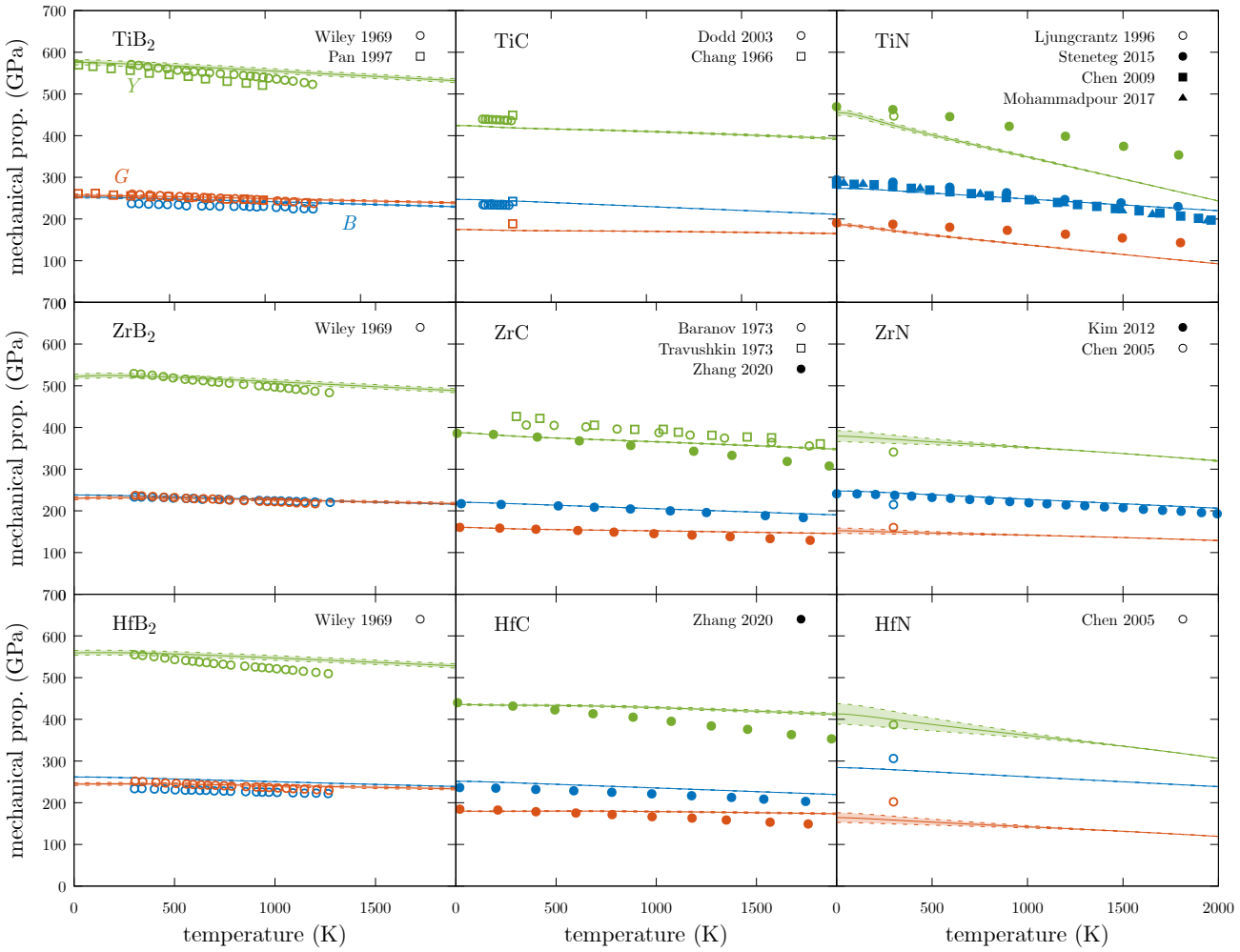


FIG. 3. Bulk modulus, $B$ (blue), Shear modulus, $G$ (orange), and Young's modulus, $Y$ (green), for UHTCs. Voigt and Reuss values are depicted with dashed lines and Voigt-Reuss-Hill values are depicted with a solid line. The area ranged between Voigt and Reuss values has also been filled with the same color than the property. Open points represent experimental measurements while filled points represent calculated values.

TABLE I. Comparison of the calculated Poisson ratio for UHTCs in this work in a 0-2000 K temperature range and experimental reported values (exp.).

| | B | | C | | N | |
|---|---|---|---|---|---|---|
| | this work | exp. | this work | exp. | this work | exp. |
| Ti | 0.11-0.12 | 0.10-0.11 [93] | 0.18-0.21 | 0.17-0.19 [104]; 0.19 [105] | 0.22-0.36 | 0.30 [104]; 0.22 [105] |
| Zr | 0.12-0.13 | 0.11-0.12 [93] | 0.18-0.21 | 0.19-0.26 [104]; 0.20 [105] | 0.23-0.25 | 0.19-0.25 [104]; 0.26 [105] |
| Hf | 0.13-0.14 | 0.12-0.13 [93] | 0.18-0.21 | 0.16-0.18 [104]; 0.16 [105] | 0.24-0.32 | 0.26-0.35 [104]; 0.17 [105] |

### E. Anisotropy

Dislocations dynamics or phase transformations are some examples in which anisotropy plays a relevant role [135]. Quantification of crystal anisotropy has been a subject of debate since Zener introduced the first anisotropy index [136]. Here, the universal elastic anisotropy index [137],

$$A^{\mathrm{U}} = \left(\frac{B_{\mathrm{V}}}{B_{\mathrm{R}}}\right) + 5\left(\frac{G_{\mathrm{V}}}{G_{\mathrm{R}}}\right) - 6, \tag{30}$$

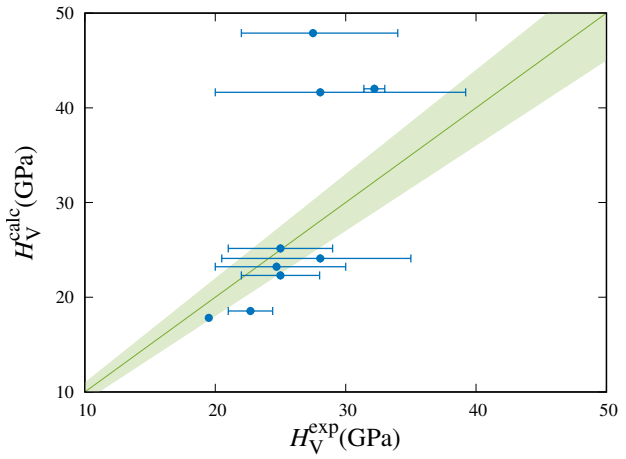


FIG. 4. Comparison between calculated, $H_V^{calc}$, and experimental, $H_V^{exp}$, hardness. Green area represent the $\mp 10\%$ relative error with respect to experimental values.

and the log-Euclidean anisotropy index [138],

$$A^L = \sqrt{\left[\ln\left(\frac{B_V}{B_R}\right)\right]^2 + 5\left[\ln\left(\frac{G_V}{G_R}\right)\right]^2}, \qquad (31)$$

are used to calculate the temperature-dependent anisotropy of UHTs (Table II).

TABLE II. Anisotroy indexes $A^U$ and $A^L$ for UHTCs in the 0-2000 K temperature range.

| | B | | C | | N | |
|---|---|---|---|---|---|---|
| | $A^U$ | $A^L$ | $A^U$ | $A^L$ | $A^U$ | $A^L$ |
| Ti | 0.13-0.11 | 0.05-0.04 | 0.03-0.09 | 0.01-0.04 | 0.19-0.00 | 0.08-0.00 |
| Zr | 0.15-0.14 | 0.06 | 0.03-0.07 | 0.01-0.03 | 0.44-0.07 | 0.19-0.03 |
| Hf | 0.14-0.13 | 0.06 | 0.05-0.11 | 0.02-0.05 | 0.76-0.02 | 0.32-0.01 |

Borides, carbides and nitrides, in general, present relatively low anisotropy indexes if they are compared with other materials [138]. While the reported $A^U$ and $A^L$ for some cubic systems can be as low as $10^{-3}$, some triclinic and monoclinic materials present $A^U$ values higher than $10^2$ [138]. Both indexes point to the nitrides as the most anisotropic materials, followed by the borides and finally the carbides (Table II). These indexes are usually obtained from 0 K calculated mechanical properties, however, their behaviour at high temperatures can be calculated using our approach. For instance, anisotropic indexes slightly increase with temperature for carbides, while they are reduced for borides and nitrides. Borides experiment change very little in their anisotropic indexes in the 0-2000 K range, however, both $A^U$ and $A^L$ are drastically reduced for nitrides.

Anisotropy indexes give relevant information about the general behavior of the material, however, some properties such as $Y$, $G$ and $\sigma$ can be directly calculated as a function of the crystallographic direction. This information is extremely valuable in order to predict the behaviour of single crystal materials in specific direction or the limits of these properties in polycrystalline samples. There are already different packages that calculate and represent the anisotropic nature of some mechanical properties [139, 140]. In this work, ELATE package [141] has be combined with our framework to explore the temperature-dependent anisotropic nature of some mechanical properties. As an example, the directional and temperature dependence of $Y$ is plotted for $TiB_2$ in Fig. 5, where $Y$ is a 33% lower in $c$ with respect to $a$ and $b$

The same approach has been followed for the rest of UHTCs materials studied in this work, not only for $Y$, but also for $G$ and $\sigma$ (Fig. 6). The colored area for each property at each temperature is delimited by the maximum and minimum values (dashed lines) predicted for $Y$ (green), $G$ (orange) and $\sigma$ (blue). Results in Fig. 6 are in good agreement with the trends extracted from anisotropy indexes. Carbides are the group of materials with a lower variability in their properties, which correspond to lower anisotropy indexes than borides and nitrides. Moreover, the difference between the maximum and minimum values in carbides slightly increases with temperature, following the same trend as the anisotropic indexes. Similarly to values in Table II, the amplitude between maximum and minimum for each property in borides remains almost constant with temperature, while a fast reduction of the amplitude can be observed for nitrides. Some singular points can be observed for nitrides, where maximum and minimum values are the same at a given temperature. These points represent an inversion in the direction where maximum and minimum values of a specific property can be observed. For instance, $Y$ maximum values is observed in the [100] direction up to 1500 K approximately. For temperatures higher than 1500 K, this trend is different and the minimum value for $Y$ is obtained in [100] direction. Same phenomena is observed in TiN and HfN around 2000 K and 1800 K, respectively. Fig. 6 is also a good approach to visualize the potential scattering in experimental measurements depending on the crystallinity, direction and temperature in which the property has been measured. Experimental data already plotted in Fig. 3 is always in between the maximum and minimum limits stablished for each property at each temperature. Only one experimental point is slightly out of the delimited area for ZrC. This very small deviation could be due to the well known underestimation of bond strength by GGA functionals.

### F. Thermodynamic and thermal properties

**Heat capacity**. Thermodynamic properties such as specific heat at constant volume, $C_V$, are calculated including phonon, $C_V^{ph}$, and electronic, $C_V^{el}$, contributions:

$$C_V = C_V^{ph} + C_V^{el}. \qquad (32)$$

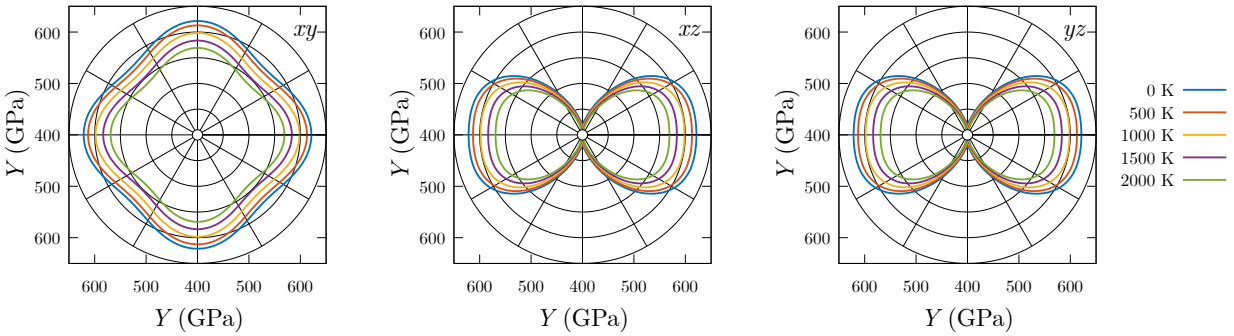


FIG. 5. Anisotropic behavior of $Y$ for $TiB_2$ at different temperatures. Left, mid and right panels correspond to $xy$, $xz$, and $yz$ planes, respectively.

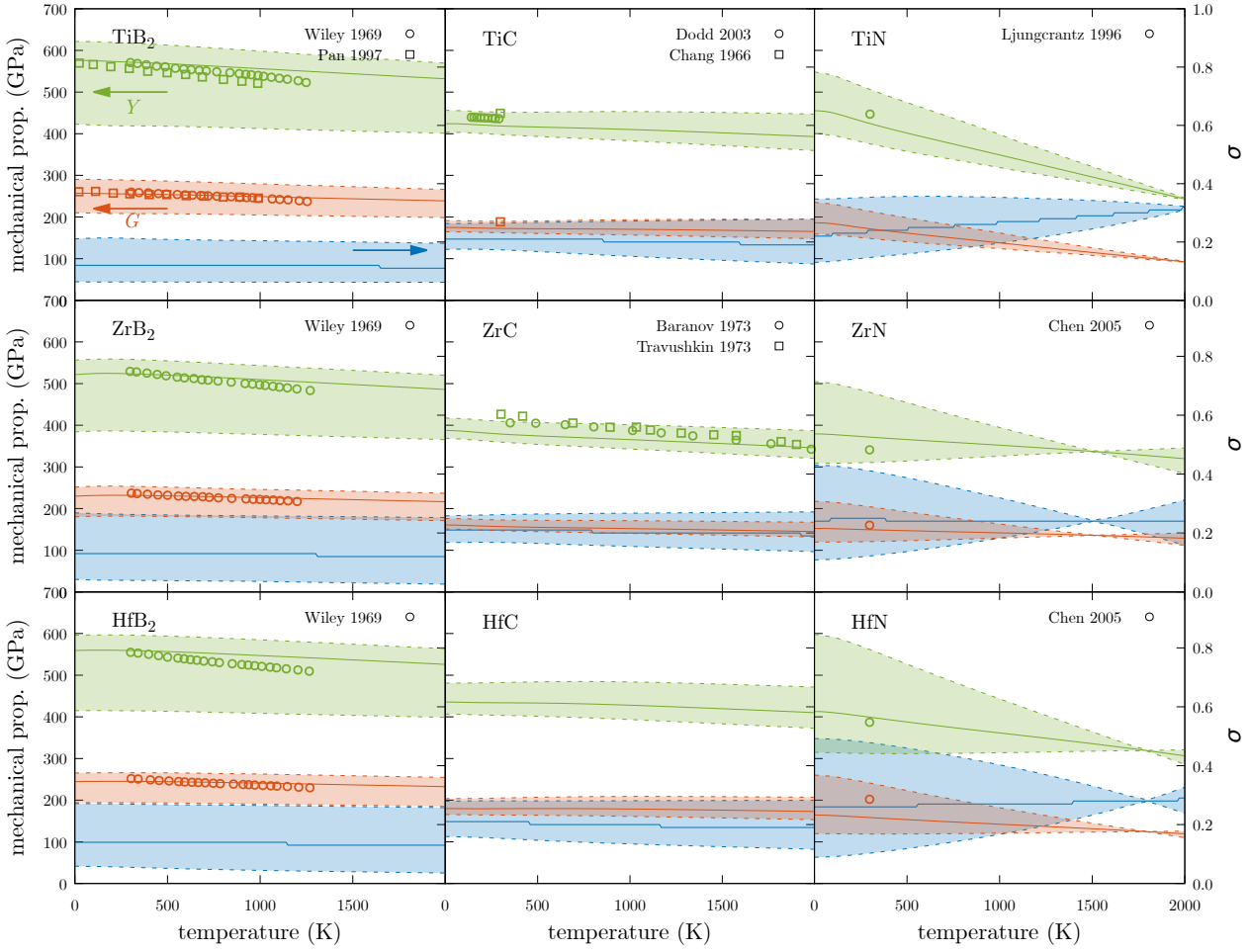


FIG. 6. Anisotropic Poisson ratio, $\sigma$ (blue), Shear modulus, $G$ (orange), and Young's modulus, $Y$ (green), for UHTCs. Solid lines represent isotropic values calculated in previous section. Dashed lines represent the upper and lower limit for each property. The area ranged between upper and lower limits has also been filled with the same color than the property. Open points represent experimental measurements.

Phonon contribution is calculated as,

$$C_V^{\rm ph} = \frac{k_{\rm B}}{N_q}\sum_{\mathbf{q},j} c_{\mathbf{q},j}, \tag{33}$$

where

$$c_{\mathbf{q},j} = \left(\frac{\hbar\omega_{\mathbf{q},j}(V_0)}{k_{\rm B}T}\right)^2 \frac{\exp\left(\frac{\hbar\omega_{\mathbf{q},j}(V_0)}{k_{\rm B}T}\right)}{\left(\exp\left(\frac{\hbar\omega_{\mathbf{q},j}(V_0)}{k_{\rm B}T}\right)-1\right)^2}. \tag{34}$$

Following the free electron gas approximation [142], the electronic contribution to heat capacity is a linear function with respect to the temperature,

$$C_V^{\mathrm{el}} = \frac{1}{3}\pi^2 N(E_{\mathrm{F}}) k_{\mathrm{B}}^2 T, \tag{35}$$

where $N(E_{\mathrm{F}})$ is the density of states (DOS) at the Fermi level. Moreover, the specific heat at constant pressure,$C_p$, which is more experimentally accesible, was calculated as [143],

$$C_p = C_V + V_{\mathrm{eq}} T B \alpha_V^2, \tag{36}$$

where $V_{\mathrm{eq}}$ is the equilibrium volumen for a given temperature and $\alpha_V$ is the volumetric lattice thermal expansion. In most cases, specific heats match experimental values well [144–153] (Fig. 7). Only small deviations, below 10% error, are found for $TiB_2$ and $HfB_2$. It has been pointed out that the origin of this difference is the importance of higher-order lattice anharmonic vibrations at higher temperatures, which are not included under the frame of the quasi-harmonic approximation [75].

**Grüneisen parameter**. Grüneisen parameter, $\gamma$, is a good measurement of the compressibility of the phonons and it is often used to estimate the anharmonicity of the vibrations in the crystal (Fig.S4). As other properties already discussed, $\gamma$ is a tensorial magnitude which depends on the direction of the tension-compression. Here, Grüneisen parameter was calculated based on an isotropic expansion-compression of the solid,

$$\bar{\gamma} = \frac{\sum_{\mathbf{q},j} \gamma_{\mathbf{q},j} c_{\mathbf{q},j}}{\sum_{\mathbf{q},j} c_{\mathbf{q},j}}, \tag{37}$$

where,

$$\gamma_{\mathbf{q},j} = \frac{V_{\mathrm{eq}}^{0K}}{2\omega_{\mathbf{q},j}^2} \sum_j e_{\mathbf{q},j} \frac{\partial D_{\mathbf{q}}}{\partial V} e_{\mathbf{q},j}. \tag{38}$$

$D_{\mathbf{q}}$ is the dynamical matrix for a wave-vector, $\mathbf{q}$, $\omega_{\mathbf{q},j}$ is the vibrational frequency, and $e_{\mathbf{q},j}$ is the eigenvector for phonon branch, $j$. The detailed procedure can be found in Refs. [27, 49]. It seems that the calculated values for borides follow the same trend as experimental results reported by Wiley *et al.* [93], with $\bar{\gamma}$ being constant over 500 K. Quantitatively, calculated values seems to slightly overestimated Wiley *et al.* results, however, values reported by Ajami *et al.* [154] and Dodd *et al.* [95] at 300 K are in good agreement with the predictions, indicating that the error of the calculation is lower than the deviation of the experimental measurements. In addition to the comparison with the experimental results, different conclusions can be extracted from Fig.S4. While no large changes are observed with the temperature for carbides and nitrides, borides present the higher dependence with respect to the temperature at low temperatures. For instance, $\bar{\gamma}$ for $ZrB_2$ is reduced up to a 30% from its maximum value at 80 K to 2000 K. If families are compared to each other, nitrides present the higher values for $\bar{\gamma}$, then carbides and finally borides.

**Thermal Expansion**. Some thermodynamic properties such as heat capacity, can be accurately obtained with low computationally demanding methods such as GIBBS [155, 156]. However, the accurate prediction of thermal expansion coefficient requires the calculation of the free energy surface which is computationally demanding. Alternatives to the standard QHA [25–27] such as QHA3P [49] can reduce the computational cost, but QHA3P has been only used for calculating volumetric thermal expansion and cannot capture the anisotropic nature of the material, when isotropic deformations are applied. The framework developed in this work fills this gap, capturing the anisotropy of the system through the calculation of linear thermal expansion coefficients and reducing the computational cost to the same level than QHA3P.

Linear and volumetric thermal expansion coefficient, $\alpha_i$, are calculated using the free energy curves obtained for the temperature-dependent elastic constants,

$$\alpha_i = \left(\frac{C_\epsilon}{V}\right) \sum_{j=1}^{6} (s_{ij})\, \gamma_j \tag{39}$$

where $C_\epsilon$ is the heat capacity at constant strain $\epsilon$, $\gamma_j$ is the Grüneisen parameter along different $j$ directions and $s_{ij}$ are the elastic compliance constants.

When the calculated values are compared with experiments (Fig. 8), good agreement was obtained for most carbides [157, 158] and nitrides [159–162], while larger deviations were found for borides [100, 162, 163]. As it is defined in Eq. 39, the $\alpha$ depends on $C_\epsilon$, $s_{ij}$ and $\gamma$. It has been proven in the previous sections that accurate values were obtained for $C_\epsilon$ and $s_{ij}$ ($c_{ij}$). However higher deviations were found for $\gamma$. Thus, the main source of error stems from the description of the anharmonicity of the material which is not completely well described by the QHA.

## IV. CONCLUSIONS

In this work, a new framework for the calculation of the thermoelastic properties of materials has been developed. The main advantage of this new approach relies on the drastic reduction of the computational cost without loosing accuracy. Ultra-high temperature ceramics have been explored within this framework because of the difficulty of experimentally obtaining their mechanical properties at temperatures close to their melting point. Very good agreement between experiments and calculations was found not only for the elastic constants but also for other mechanical properties such as $B$, $G$, $Y$, or $\sigma$. Although hardness is a property that also depends on plastic deformation, good trends were also predicted. While approximations or frameworks with similar computational cost only predict isotropic or averaged properties, this new approach also predicts anisotropic properties describing directional mechanical properties such as $Y$ or establishing upper and

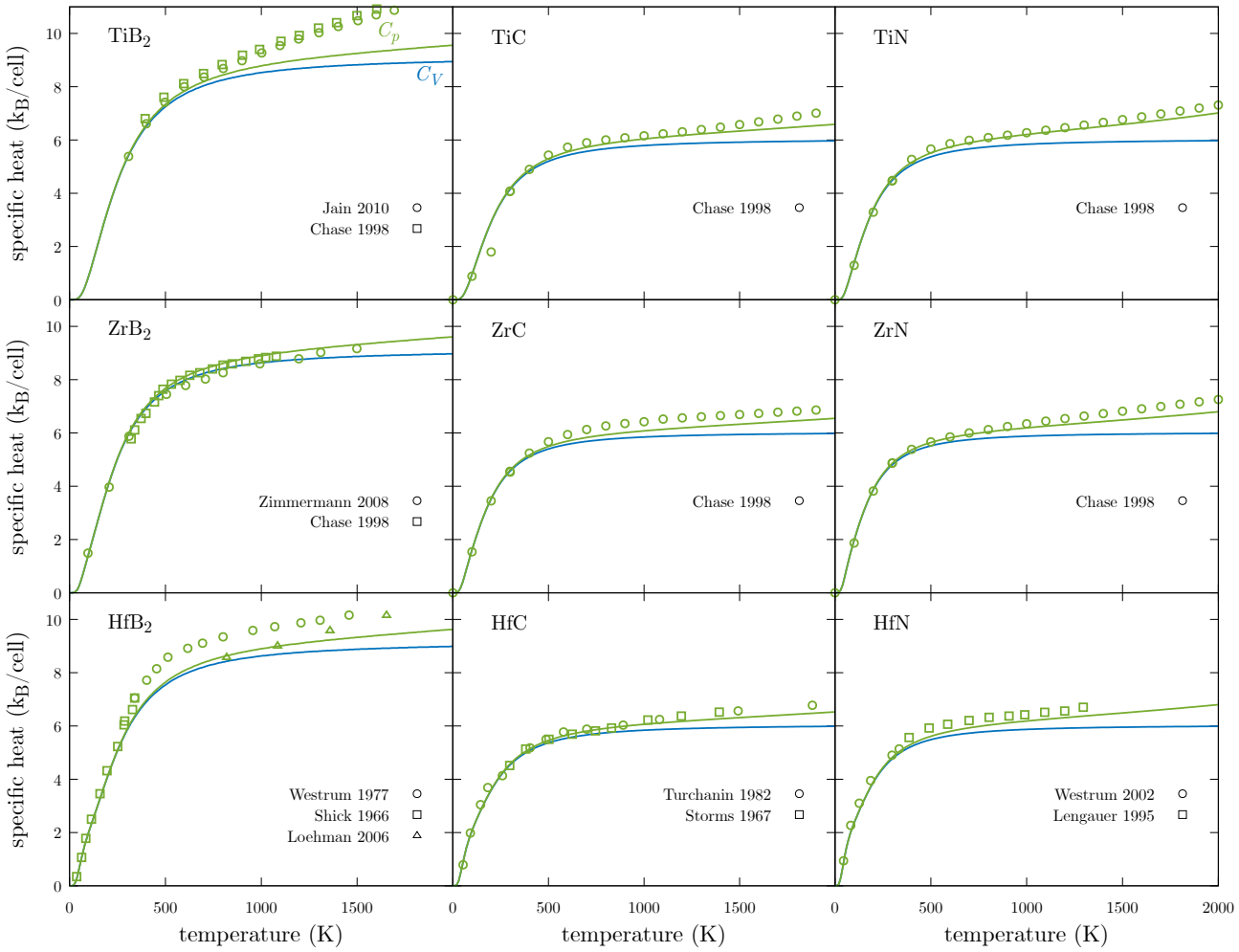


FIG. 7. Heat capacity at constant volume, $C_V$ (blue), and at constant pressure, $C_p$ (green) for UHTCs. Solid lines represent calculated values while open points represent experimental measurements.

lower limits for polycrystalline materials. Thermodynamical and thermal properties were also explored, obtaining, in most cases, good agreement with available experimental data.

This new approach is a perfect tool for the systematic exploration of the thermoelastic properties of crystalline materials, because of the substantial reduction of the computational cost. Moreover, this framework can be considered as a starting point for the development of more elaborated methods in order to solve some deficiencies, such as the inclusion of anharmonic effects or the exploration of more complex systems, such as solid solutions.

## CONFLICTS OF INTEREST

There are no conflicts to declare.

## ACKNOWLEDGMENTS

This work was funded by the Ministerio de Ciencia e Innovación (PID2019-106871GB-I00), and European Union´s Horizon 2020 research and innovation programme under the Marie Sklodowska-Curie grant agreement HT-PHOTO-DB No 752608. The authors thankfully acknowledge the computer resources at Lusitania and the technical support provided by Cénits-COMPUTAEX and Red Española de Supercomputación, RES (QS-2019-2-0006, QS-2019-3-0021, QS-2020-2-0033).

[1] E. Wuchina, E. Opila, M. Opeka, W. Fahrenholtz, and I. Talmy, *UHTCs: Ultra-High Temperature Ceramic materials for extreme environment applications*, Electrochem-

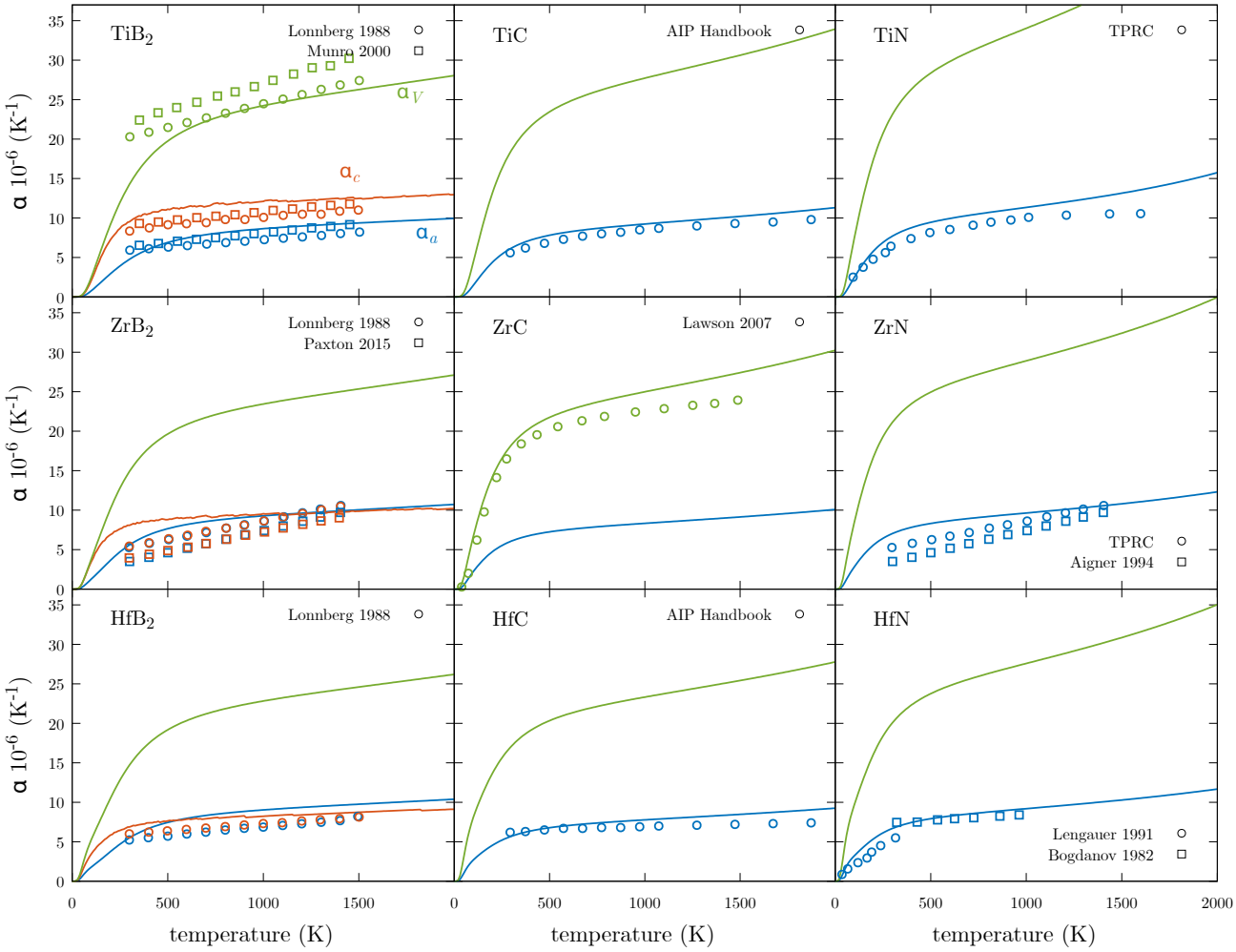


FIG. 8. Volumetric thermal expansión coefficient, $\alpha_V$ (green), and linear thermal expansión coefficients, $\alpha_a$ (blue) and $\alpha_c$ (orange) for UHTCs. Solid lines represent calculated values while open points represent experimental measurements.


ical Society, Inc. **16**, 30 (2007).

[2] W. G. Fahrenholtz, E. J. Wuchina, W. E. Lee, and Y. Zhou, *Ultra-High Temperature Ceramics: Materials for extreme environments Applications* (Wiley, New York, 2014), 1 edn.

[3] W. G. Fahrenholtz and G. E. Hilmas, *Ultra-high temperature ceramics: Materials for extreme environments*, Scr. Mater. **129**, 94 (2017).

[4] H. Moissan, *Sur un nouveau carbure de zirconium*, Comptes rendus hebdomadaires des séances de l Académie des Sciences **122**, 651 (1896).

[5] S. A. Tucker and H. R. Moody, *II. - The production of hitherto unknown metallic borides*, J. Chem. Soc., Trans. **81**, 14–17 (1902).

[6] D. Kalish, E. V. Clougherty, and K. Kreder, *Strength, Fracture Mode, and Thermal Stress Resistance of $HfB_2$ and $ZrB_2$*, J. Am. Ceram. Soc. **52**, 30 (1969).

[7] S. R. Levine, E. J. Opila, M. C. Halbig, J. D. Kiser, M. Singh, and J. A. Salem, *Evaluation of ultra-high temperature ceramics for aeropropulsion use*, J. Eur. Ceram. Soc. **22**, 2757 (2002).

[8] D. M. V. Wie, D. Drewry, D. E. King, and C. M. Hudson, *The hypersonic environment: Required operating conditions and design challenges*, J. Mater. Sci. **39**, 5915 (2004).

[9] M. M. Opeka, I. G. Talmy, E. J. Wuchina, J. A. Zaykoski, and S. J. Causey, *Mechanical, Thermal, and Oxidation Properties of Refractory Hafnium and zirconium Compounds*, J. Eur. Ceram. Soc. **19**, 2405 (1999).

[10] X. Zhang, X. Luo, J. Han, J. L., and W. Han, *Electronic structure, elasticity and hardness of diborides of zirconium and hafnium: First principles calculations*, Comput. Mater. Sci. **44**, 411 (2008).

[11] A. L. Chamberlain, W. G. Fahrenholtz, G. E. Hilmas, and D. T. Ellerby, *High-strength zirconium diboride-based ceramics*, J. Am. Ceram. Soc. **87**, 1170–1172 (2004).

[12] M. Gasch, D. Ellerby, E. Irby, S. Beckman, M. Gusman, and S. Johnson, *Processing, properties and arc jet oxidation of hafnium diboride/silicon carbide ultra high temperature ceramics*, J. Mater. Sci. **39**, 5925–5937 (2004).

[13] S. Tang, J. Deng, S. Wang, W. Liu, and K. Yang, *Ablation behaviors of ultra-high temperature ceramic composites*, Mater. Sci. Eng. A **465**, 1 (2007).

[14] F. Monteverde, A. Bellosi, and L. Scatteia, *Processing and properties of ultra-high temperature ceramics for space applications*, Mater. Sci. Eng. A **485**, 415 (2008).

[15] J. Han, P. Hu, X. Zhang, S. Meng, and W. Han, *Oxidation-resistant $ZrB_2$-SiC composites at 2200 °C*, Compos. Sci. Technol. **68**, 799 (2008).

[16] H. F. Jackson, D. D. Jayaseelan, D. Manara, C. P. Casoni, and W. E. Lee, *Laser Melting of Zirconium Carbide: Determination of Phase Transitions in Refractory Ceramic Systems*, J. Am. Ceram. Soc. **94**, 3561 (2011).

[17] E. W. Neuman, G. E. Hilmas, and W. G. Fahrenholtz, *Strength of Zirconium Diboride to 2300 °C*, J. Am. Ceram. Soc. **96**, 47 (2013).

[18] M. Miller-Oana, P. Neff, M. Valdez, A. Powell, M. Packard, L. S. Walker, and E. L. Corral, *Oxidation Behavior of Aerospace Materials in High Enthalpy Flows Using an Oxyacetylene Torch Facility*, J. Am. Ceram. Soc. **98**, 1300 (2015).

[19] A. Paul, J. G. P. Binner, B. Vaidhyanathan, A. C. J. Heaton, and P. M. Brown, *Heat flux mapping of oxy-acetylene flames and their use to characterise Cf-$HfB_2$ composites*, Adv. Appl. Ceram **115**, 158 (2016).

[20] Z. Erjun and W. Zhijian, *Electronic and mechanical properties of 5d transition metal mononitrides via first principles*, J. Solid State Chem. **181**, 2814 (2008).

[21] J. D. Zhang, X. L. Cheng, and D. H. Li, *First-principles study of the elastic and thermodynamic properties of $HfB_2$ with $AlB_2$ structure under high pressure*, J. Alloy. Compd. **509**, 9577 (2011).

[22] Q. Zeng, J. Peng, A. R. Oganov, Q. Zhu, C. Xie, X. Zhang, D. Dong, L. Zhang, and L. Cheng, *Prediction of stable hafnium carbides: Stoichiometries, mechanical properties, and electronic structure*, Phys. Rev. B **88**, 214107 (2013).

[23] T. Cheng and W. Li, *The Temperature-Dependent Ideal Tensile Strength of $ZrB_2$, $HfB_2$, and $TiB_2$*, J. Am. Ceram. Soc. **98**, 190 (2015).

[24] H. Xiang, Z. Feng, Z. Li, and Y. Zhou, *First-principles investigations on elevated temperature elastic and thermodynamic properties of $ZrB_2$ and $HfB_2$*, J. Am. Ceram. Soc. **100**, 3662 (2017).

[25] P. Carrier, R. Wentzcovitch, and J. Tsuchiya, *First-principles prediction of crystal structures at high temperatures using the quasiharmonic approximation*, Phys. Rev. B **76**, 064116 (2007).

[26] S. Baroni, P. Giannozzi, and E. Isaev, *Density-Functional Perturbation Theory for Quasi-Harmonic Calculations*, Rev. Mineral Geochem. **71**, 39–57 (2010).

[27] P. Nath, J. J. Plata, D. Usanmaz, R. Al Rahal Al Orabi, M. Fornari, M. Buongiorno Nardelli, C. Toher, and S. Curtarolo, *High-throughput prediction of finite-temperature properties using the quasi-harmonic approximation*, Comput. Mater. Sci. **125**, 82–91 (2016).

[28] R. Golesorkhtabar, P. Pavone, J. Spitaler, P. Puschnig, and C. Draxl, *ElaStic: A tool for calculating second-order elastic constants from first principles*, Comput. Phys. Commun. **184**, 1861–1873 (2013).

[29] J. Zhao, J. M. Winey, and Y. M. Gupta, *First-principles calculations of second- and third-order elastic constants for single crystals of arbitrary symmetry*, Phys. Rev. B **75**, 094105 (2007).

[30] G. F. Davies, *Effective elastic moduli under hydro-static stress-I. Quasiharmonic theory*, J. Phys. Chem. Solids **35**, 1513–1520 (1974).

[31] B. B. Karki, R. M. Wentzcovitch, S. D. Gironcoli, and S.Baroni, *First-principles determination of elastic anisotropy and wave velocities of MgO at lower mantle conditions*, Science **286**, 1705–1707 (1999).

[32] B. Karki, R. Wentzcovitch, S. de Gironcoli, and S. Baroni, *High-pressure lattice dynamics and thermoelasticity of MgO*, Phys. Rev. B **61**, 8793–8800 (2000).

[33] Z. Wu and R. M. Wentzcovitch, *Quasiharmonic thermal elasticity of crystals: An analytical approach*, Phys. Rev. B **83** (2011).

[34] K. Kádas, L. Vitos, R. Ahuja, B. Johansson, and J. Kollár, *Temperature-dependent elastic properties of $\alpha$-beryllium from first principles*, Phys. Rev. B **76**, 235109 (2007).

[35] Y. Wang, J. J. Wang, H. Zhang, V. R. Manga, S. L. Shang, L. Q. Chen, and Z. K. Liu, *A first-principles approach to finite temperature elastic constants*, J. Phys.: Condens. Matter **22**, 225404 (2010).

[36] G. Liu, Z. Gao, and J. Ren, *Anisotropic thermal expansion and thermodynamic properties of monolayer $\beta$-Te*, Phys. Rev. B **99**, 195436 (2019).

[37] G. Liu, H. Wang, G. L. Li, and D. Wang, *Giant anisotropy of thermal expansion and thermomechanical properties of monolayer $\alpha$-antimonene: A first-principles study*, Comput. Mater. Sci. **169**, 109132 (2019).

[38] M. Destefanis, C. Ravoux, A. Cossard, and A. Erba, *Thermo-Elasticity of Materials from Quasi-Harmonic Calculations*, Minerals **9**, 16 (2019).

[39] D. C. Wallace, *Thermodynamics of crystals* (Wiley, 1972).

[40] S. H. Zhang and R. F. Zhang, *AELAS: Automatic ELAStic property derivations via high-throughput first-principles computation*, Comput. Phys. Commun. **220**, 403 (2017).

[41] G. Liu, Z. Gao, and J. Ren, *Anisotropic thermal expansion and thermodynamic properties of monolayer $\beta$-Te*, Phys. Rev. B **99**, 195436 (2019).

[42] O. H. Nielsen and R. M. Martin, *First-Principles Calculation of Stress*, Phys. Rev. Lett. **50**, 697–700 (1983).

[43] M. de Jong, W. Chen, T. Angsten, A. Jain, R. Notestine, A. Gamst, M. Sluiter, C. K. Ande, S. van der Zwaag, J. J. Plata, C. Toher, S. Curtarolo, G. Ceder, K. A. Persson, and M. D. Asta, *Charting the Complete Elastic properties of Inorganic Crystalline Compounds*, Sci. Data **2**, 150009 (2015).

[44] Z. K. Liu and Y. Wang, *Computational Thermodynamics of Materials* (Cambridge University Press, 2016), 1 edn.

[45] Y. Wang, Z.-K. Liu, and L.-Q. Chen, *Thermodynamic properties of Al, Ni, NiAl, and $Ni_3Al$ from first-principles calculations*, Acta Mater. **52**, 2665–2671 (2004).

[46] T. Duong, S. Gibbons, R. Kinra, and R. Arróyave, *Ab-initio approach to the electronic, structural, elastic, and finite-temperature thermodynamic properties of $Ti_2AX$ ($A$ = Al or Ga and $X$ = C or N)*, J. Appl. Phys. **110**, 093504 (2011).

[47] G. Kresse and J. Furthmüller, *Efficient iterative schemes for ab initio total-energy calculations using a plane-wave basis set*, Phys. Rev. B **54**, 11169–11186 (1996).

[48] P. Giannozzi, S. Baroni, N. Bonini, M. Calandra, R. Car, C. Cavazzoni, D. Ceresoli, G. L. Chiarotti, M. Cococcioni, I. Dabo, A. Dal Corso, S. de Gironcoli, S. Fabris, G. Fratesi, R. Gebauer, U. Gerstmann, C. Gougoussis, A. Kokalj, M. Lazzeri, L. Martin-Samos, N. Marzari, F. Mauri, R. Mazzarello, S. Paolini, A. Pasquarello, L. Paulatto, C. Sbraccia, S. Scandolo, G. Sclauzero, A. P. Seitsonen, A. Smogunov, P. Umari, and R. M. Wentzcovitch, *QUANTUM ESPRESSO: a modular and open-source software project for quantum simulations of materials*, J. Phys.: Condens. Matter **21**, 395502 (2009).

[49] P. Nath, D. Usanmaz, D. Hicks, C. Oses, M. Fornari, M. N. Buongiorno, C. Toher, and S. Curtarolo, *AFLOW-QHA3P/: Robust and automated method to compute thermodynamic properties of solids*, Phys. Rev. Materials **3**, 073801 (2019).

[50] A. Togo and I. Tanaka, *First principles phonon calculations in materials science*, Scr. Mater. **108**, 1–5 (2015).

[51] R. Arroyave, D. Shin, and Z.-K. Liu, *Ab initio thermodynamic properties of stoichiometric phases in the Ni-Al system*, Acta Mater. **53**, 1809–1819 (2005).

[52] L. F. Huang, X. Z. Lu, E. Tennessen, and J. M. Rondinelli, *An efficient ab-initio quasiharmonic approach for the thermodynamics of solids*, Comput. Mater. Sci. **120**, 84–93 (2016).

[53] F. H. Featherston and J. R. Neighbours, *Elastic Constants of Tantalum, Tungsten, and Molybdenum*, Phys. Rev. **130**, 1324–1333 (1963).

[54] T. Davenport, L. Zhou, and J. Trivisonno, *Ultrasonic and atomic force studies of the martensitic transformation induced by temperature and uniaxial stress in NiAl alloys*, Phys. Rev. B **59**, 3421–3426 (1999).

[55] M. Basaadat and M. Payami, *Elastic stiffness tensors of Zr–xNb alloy in the presence of defects: A molecular dynamics study*, Int. J. Mod. Phys. C **0**, 2050028 (0).

[56] *Spglib for Python*, https://atztogo.github.io/spglib/python-spglib.html (2017).

[57] G. Kresse and J. Hafner, *Ab initio molecular dynamics for liquid metals*, Phys. Rev. B **47**, 558–561 (1993).

[58] P. E. Blöchl, *Projector augmented-wave method*, Phys. Rev. B **50**, 17953–17979 (1994).

[59] J. P. Perdew, K. Burke, and M. Ernzerhof, *Generalized Gradient Approximation Made Simple*, Phys. Rev. Lett. **77**, 3865–3868 (1996).

[60] C. E. Calderon, J. J. Plata, C. Toher, C. Oses, O. Levy, M. Fornari, A. Natan, M. J. Mehl, G. L. W. Hart, M. Buongiorno Nardelli, and S. Curtarolo, *The AFLOW standard for high-throughput materials science calculations*, Comput. Mater. Sci. **108 Part A**, 233–238 (2015).

[61] T. Tadano, Y. Gohda, and S. Tsuneyuki, *Anharmonic force constants extracted from first-principles molecular dynamics: applications to heat transfer simulations*, J. Phys.: Condens. Matter **26**, 225402 (2014).

[62] J. J. Plata, P. Nath, D. Usanmaz, J. Carrete, C. Toher, M. de Jong, M. D. Asta, M. Fornari, M. Buongiorno Nardelli, and S. Curtarolo, *An efficient and accurate framework for calculating lattice thermal conductivity of solids: AFLOW-AAPL Automatic Anharmonic Phonon Library*, NPJ Comput. Mater. **3**, 45 (2017).

[63] D. Alfé, *PHON: A program to calculate phonons using the small displacement method*, Comput. Phys. Commun. **180**, 2622–2633 (2009).

[64] E. I. Isaev, S. I. Simak, I. A. Abrikosov, R. Ahuja, Y. K. Vekilov, M. I. Katsnelson, A. I. Lichtenstein, and B. Johansson, *Phonon related properties of transition metals, their carbides, and nitrides: A first-principles study*, J. Appl. Phys. **101**, 123519 (2007).

[65] T. Aizawa, W. Hayami, and S. Otani, *Surface phonon dispersion of* $ZrB_2(0001)$ *and* $NbB_2(0001)$, Phys. Rev. B **65**, 024303 (2001).

[66] L. Pintschovius, W. Reichardt, and B. Scheerer, *Lattice dynamics of TiC*, J. Phys. C: Solid State Phys. **11**, 1557–1562 (1978).

[67] W. Kress, P. Roedhammer, H. Bilz, W. D. Teuchert, and A. N. Christensen, *Phonon anomalies in transition-metal nitrides: TiN*, Phys. Rev. B **17**, 111–113 (1978).

[68] W. Weber, *Lattice Dynamics of Transition-Metal Carbides*, Phys. Rev. B **8**, 5082–5092 (1973).

[69] A. N. Christensen, O. W. Dietrich, W. Kress, and W. D. Teuchert, *Phonon anomalies in transition-metal nitrides: ZrN*, Phys. Rev. B **19**, 5699–5703 (1979).

[70] A. N. Christensen, W. Kress, M. Miura, and N. Lehner, *Phonon anomalies in transition-metal nitrides: HfN*, Phys. Rev. B **28**, 977–981 (1983).

[71] H. G. Smith and W. Glazer, in *Proceedings of the International Conference on Phonons*, edited by M. A. Nusimovici (Wiley, Rennes, Frances, 1971).

[72] H. G. Smith, *Phonon Anomalies in Transition-Metal Carbides*, Phys. Rev. Lett. **29**, 353–354 (1972).

[73] N. L. Okamoto, M. Kusakari, K. Tanaka, H. Inui, M. Yamaguchi, and S. Otani, *Mechanical and thermal properties of single crystals of* $ZrB_2$ (2003), vol. 753, pp. 83–88.

[74] N. L. Okamoto, M. Kusakari, K. Tanaka, H. Inui, and S. Otani, *Anisotropic elastic constants and thermal expansivities in monocrystal* $CrB_2$*,* $TiB_2$*, and* $ZrB_2$, Acta Mater. **58**, 76 – 84 (2010).

[75] H. Xiang, Z. Feng, Z. Li, and Y. Zhou, *Temperature-dependence of structural and mechanical properties of* $TiB_2$*: A first principle investigation*, J. Appl. Phys. **117**, 225902 (2015).

[76] R. Chang and L. J. Graham, *Low-Temperature Elastic Properties of ZrC and TiC*, J. Appl. Phys. **37**, 3778–3783 (1966).

[77] X. J. Chen, V. V. Struzhkin, Z. Wu, M. Somayazulu, J. Qian, S. Kung, A. N. Christensen, Y. Zhao, R. E. Cohen, H. Mao, and R. J. Hemley, *Hard superconducting nitrides*, Proc. Natl. Acad. Sci. **102**, 3198–3201 (2005).

[78] D. Holec, M. Friák, J. Neugebauer, and P. H. Mayrhofer, *Trends in the elastic response of binary early transition metal nitrides*, Phys. Rev. B **85**, 064101 (2012).

[79] P. Steneteg, O. Hellman, O. Y. Vekilova, N. Shulumba, F. Tasnádi, and A. Abrikosov, *Temperature dependence of TiN elastic constants from ab initio molecular dynamics simulations*, Phys. Rev. B **87**, 094114 (2013).

[80] J. Zhang and J. M. McMahon, *Temperature-dependent mechanical properties of ZrC and HfC from first principles* (2020).

[81] B. B. Karki, G. J. Ackland, and J. Crain, *Elastic instabilities in crystals from ab initio stress–strain relations*, J. Phys.: Condens. Matter **9**, 8579–8589 (1997).

[82] M. Born and K. Huang, *Dynamic Theory of Crystal Lattices* (Oxfird University Press., Oxford, 1954).

[83] J. Wang, S. Yip, S. R. Phillpot, and D. Wolf, *Crystal instabilities at finite strain*, Phys. Rev. Lett. **71**, 4182 (1993).

[84] J. F. Nye, *Physical Properties of Crystals: Their Representation by Tensors and Matrices* (Oxfird University Press., Oxford, 1985).

[85] F. Mouhat and F. X. Coudert, *Necessary and sufficient elastic stability conditions in various crystal systems*, Phys. Rev. B **90**, 224104 (2014).

[86] W. Voigt, *Lehrbuch der Kristallphysik* (Teubner, Leipsig, 1928).

[87] A. Reuss, *Berechnung der Fließgrenze von Mischkristallen auf Grund der Plastizitätsbedingung für Einkristalle*, Z. Angew. Math. Mech. **9**, 49–58 (1929).

[88] R. Hill, *The elastic behaviour of a crystalline aggregate*, Proc. Phys. Soc. **65**, 349–354 (1952).

[89] R. M. Spriggs, *Expression for Effect of Porosity on Elastic Modulus of Polycrystalline Refractory Materials, Particularly Aluminum Oxide*, J. Amer. Ceram. Soc. **44**, 628–629 (1961).

[90] S. C. Nanjangud, R. Brezny, and D. J. Green, *Strength and Young's Modulus Behavior of a Partially Sintered Porous Alumina*, J. Amer. Ceram. Soc. **78**, 266–268 (1995).

[91] R. W. Rice, *The Porosity Dependence of Physical Properties of Materials: A Summary Review*, Key Eng. Mat. **115**, 1–20 (1996).

[92] I. J. Gibson and M. F. Ashby, *The mechanics of three-dimensional cellular materials*, Proc. R. Soc. Lond. A. Math. Phy. **382**, 43–59 (1982).

[93] D. E. Wiley, W. R. Manning, and O. Hunter, *Elastic properties of polycrystalline $TiB_2$, $ZrBi_2$ and $HfB_2$ from room temperature to 1300 K*, J. Less-Common Met. **18**, 149 – 157 (1969).

[94] M. J. Pan, P. A. Hoffman, D. J. Green, and J. R. Hellmann, *Elastic Properties and Microcracking Behavior of Particulate Titanium Diboride–Silicon Carbide Composites*, J. Amer. Ceram. Soc. **80**, 692–698 (1997).

[95] S. P. Dodd, M. Cankurtaran, and B. James, *Ultrasonic determination of the elastic and nonlinear acoustic properties of transition-metal carbide ceramics: TiC and TaC*, J. Mater. Sci. **38**, 1107–1115 (2003).

[96] D. Chen, J. Chen, Y. Zhao, B. Yu, C. Wang, and D. Shi, *Theoretical study of the elastic properties of titanium nitride*, Acta Metall. Sin.-Engl. **22**, 146 – 152 (2009).

[97] E. Mohammadpour, M. Altarawneh, J. Al-Nu'airat, Z. T. Jiang, N. Mondinos, and B. Z. Dlugogorski, *Thermo-mechanical properties of cubic titanium nitride*, Mol. Simulat. **44**, 415–423 (2018).

[98] J. Kim and S. Kang, *First principles investigation of temperature and pressure dependent elastic properties of ZrC and ZrN using Debye-Gruneisen theory*, J. Alloys Compd. **540**, 94 – 99 (2012).

[99] P. S. Spoor, J. D. Maynard, M. J. Pan, D. J. Green, J. R. Hellmann, and T. Tanaka, *Elastic constants and crystal anisotropy of titanium diboride*, Appl. Phys. Lett. **70**, 1959–1961 (1997).

[100] R. G. Munro, *Material Properties of Titanium Diboride*, J. Res. Natl. Inst. Stand. Technol. **105**, 709–720 (2000).

[101] V. M. Baranov, V. I. Knyazev, and O. S. Korostin, *The temperature dependence of the elastic constants of nonstoichiometric zirconium carbides*, Strength Mater. **5**, 1074–1077 (1973).

[102] G. G. Travushkin, V. I. Knyazev, V. S. Belov, and G. A. Rymashevskii, *Temperature threshold of brittle failure in interstitial phases*, Strength Mater. **5**, 639–641 (1973).

[103] H. Ljungcrantz, M. Odén, L. Hultman, J. E. Greene, and J. E. Sundgren, *Nanoindentation studies of single-crystal (001)-, (011)-, and (111)-oriented TiN layers on MgO*, J. Appl. Phys. **80**, 6725–6733 (1996).

[104] C. Kral, W. Lengauer, D. Rafaja, and P. Ettmayer, *Critical review on the elastic properties of transition metal carbides, nitrides and carbonitrides*, J. Alloys Compd. **265**, 215–233 (1998).

[105] Q. Yang, W. Lengauer, T. Koch, M. Scheerer, and I. Smid, *Hardness and elastic properties of $Ti(C_xN_{1-x})$, $Zr(C_xN_{1-x})$ and $Hf(C_xN_{1-x})$*, J. Alloys Compd. **309**, L5–L9 (2000).

[106] Y. V. Milman, S. I. Chugunova, I. V. Goncharova, T. Chudoba, W. Lojkowski, and W. Gooch, *Temperature dependence of hardness in silicon–carbide ceramics with different porosity*, Int. J. Refract. Met. H. **17**, 361 – 368 (1999).

[107] R. W. Rice, C. C. Wu, and F. Boichelt, *Hardness–Grain-Size Relations in Ceramics*, J. Amer. Ceram. Soc. **77**, 2539–2553 (1994).

[108] J. Gong, H. Miao, Z. Zhao, and Z. Guan, *Load-dependence of the measured hardness of Ti(C,N)-based cermets*, Mat. Sci. Eng. A **303**, 179 – 186 (2001).

[109] B. Guo, L. Zhang, L. Cao, T. Zhang, F. Jiang, and L. Yan, *The correction of temperature-dependent Vickers hardness of cemented carbide base on the developed high-temperature hardness tester*, J. Mater. Process. Technol. **255**, 426 – 433 (2018).

[110] F. Gao, J. He, E. Wu, S. Liu, D. Yu, D. Li, S. Zhang, and Y. Tian, *Hardness of Covalent Crystals*, Phys. Rev. Lett. **91**, 015502 (2003).

[111] A. Šimůnek and J. Vackář, *Hardness of Covalent and Ionic Crystals: First-Principle Calculations*, Phys. Rev. Lett. **96**, 085501 (2006).

[112] X. Q. Chen, H. Niu, D. Li, and Y. Li, *Modeling hardness of polycrystalline materials and bulk metallic glasses*, Intermetallics **19**, 1275–1281 (2011).

[113] X.-Q. Chen, H. Niu, C. Franchini, D. Li, and Y. Li, *Hardness of T-carbon: Density functional theory calculations*, Phys. Rev. B **84**, 121405 (2011).

[114] Y. Tian, B. Xu, and Z. Zhao, *Microscopic theory of hardness and design of novel superhard crystals*, Int. J. Refract. Met. Hard Mater. **33**, 93–106 (2012).

[115] J. F. Shackelford, Y. H. Han, S. Kim, and S. H. Kwon, *CRC Materials Science and Engineering Handbook* (CRC Press, New York, 2015).

[116] S. Otani, *High Temperature Hardness and Flux Growth of $TiB_2$, $VB_2$ and $CrB_2$ Crystals*, J. Ceram. Soc. Jpn. **108**, 955–956 (2000).

[117] G. B. Raju, B. Basu, N. H. Tak, and S. J. Cho, *Temperature dependent hardness and strength properties of $TiB_2$ with $TiSi_2$ sinter-aid*, J. Eur. Ceram. Soc. **29**, 2119 – 2128 (2009).

[118] W. G. Fahrenholtz, G. E. Hilmas, I. G. Talmy, and J. A. Zaykoski, *Refractory Diborides of Zirconium and Hafnium*, J. Amer. Ceram. Soc. **90**, 1347–1364 (2007).

[119] Y. Xuan, C. H. Chen, and S. Otani, *High temperature microhardness of $ZrB_2$ single crystals*, J. Phys. D: Appl. Phys. **35**, L98–L100 (2002).

[120] T. Csanádi, S. Grasso, A. Kovalčíková, J. Dusza, and M. Reece, *Nanohardness and elastic anisotropy of $ZrB_2$ crystals*, J. Eur. Ceram. Soc. **36**, 239 – 242 (2016).

[121] L. Bsenko and T. Lundström, *The high-temperature hardness of $ZrB_2$ and $HfB_2$*, J. Less-Common Met. **34**, 273 – 278 (1974).

[122] H. Liang, S. Guan, X. Li, A. Liang, Y. Zeng, C. Liu, H. Chen, W. Lin, D. He, L. Wang, and F. Peng, *Microstructure evolution, densification behavior and mechanical properties of nano-$HfB_2$ sintered under high pressure*, Ceram. Int. **45**, 7885 – 7893 (2019).

[123] Y. Kumashiro, A. Itoh, T. Kinoshita, and M. Sobajima, *The micro-Vickers hardness of TiC single crystals up to 1500 °C*, J. Mater. Sci. **12**, 595–601 (1977).

[124] C. Maerky, M. O. Guillou, J. L. Henshall, and R. M. Hooper, *Indentation hardness and fracture toughness in single crystal $TiC_{0.96}$*, Mat. Sci. Eng. A **209**, 329 – 336 (1996).

[125] D. L. Kohlstedt, *The temperature dependence of microhardness of the transition-metal carbides*, J. Mater. Sci. **8**, 777 – 786 (1973).

[126] Y. Kumashiro, Y. Nagai, and H. Kato, *The Vickers microhardness of NbC, ZrC and TaC single crystals up to 1500*, J. Mater. Sci. Lett. **1**, 49 – 52 (1982).

[127] J. Balko, T. Csanádi, R. Sedlák, M. Vojtko, A. Koval-Líková, K. Koval, P. Wyzga, and A. N. Duszová, *Nanoindentation and tribology of VC, NbC and ZrC refractory carbides*, J. Eur. Ceram. Soc. **37**, 4371 – 4377 (2017).

[128] E. J. Cheng, Y. Li, J. Sakamoto, S. Han, H. Sun, J. Noble, H. Katsui, and T. Goto, *Mechanical properties of individual phases of $ZrB_2$-ZrC eutectic composite measured by nanoindentation*, J. Eur. Ceram. Soc. **37**, 4223 – 4227 (2017).

[129] M. Bauccio, ed., *ASM Engineered Materials Reference Book* (ASM International, Materials Park, Ohio, USA, 1994).

[130] R. A. Andrievski, *Physical-mechanical properties of nanostructured titanium nitride*, Nanostruc. Mater. **9**, 607 – 610 (1997).

[131] A. B. Mei, B. M. Howe, C. Zhang, M. Sardela, J. N. Eckstein, L. Hultman, A. Rockett, I. Petrov, and J. E. Greene, *Physical properties of epitaxial ZrN/MgO(001) layers grown by reactive magnetron sputtering*, J. Vac. Sci. Technol. A **31**, 061516 (2013).

[132] A. G. Atkins and D. Tabor, *Hardness and deformation properties of solids at very high temperatures*, Proc. Roy. Soc. A **292**, 441–459 (1966).

[133] A. G. Atkins, A. Silverio, and D. Tabor, J. Inst. Metals **94**, 369 (1966).

[134] C. H. Chen, Y. Xuan, and S. Otani, *Temperature and loading time dependence of hardness of $LaB_6$, $YB_6$ and TiC single crystals*, J. Alloys Compd. **350**, L4 – L6 (2003).

[135] H. Ledbetter and A. Migliori, *A general elastic-anisotropy measure*, J. Appl. Phys. **100**, 063516 (2006).

[136] C. Zener, *Elasticity and Aneslaticity of Metals* (University of Chicago, Chicago, 1948).

[137] S. I. Ranganathan and M. Ostoja-Starzewski, *Universal Elastic Anisotropy Index*, Phys. Rev. Lett. **101**, 055504 (2008).

[138] C. C. M. Kube, *Elastic anisotropy of crystals*, AIP Adv. **6**, 095209 (2016).

[139] A. Marmier, Z. A. D. Lethbridge, R. I. Walton, C. W. Smith, S. C. Parker, and K. E. Evans, *ElAM: A computer program for the analysis and representation of anisotropic elastic properties*, Comput. Phys. Commun. **181**, 2102 – 2115 (2010).

[140] A. U. Ortiz, , A. Boutin, A. H. Fuchs, and F. X. Coudert, *Metal–organic frameworks with wine-rack motif: What determines their flexibility and elastic properties?*, J. Chem. Phys. **138**, 174703 (2013).

[141] R. Gaillac, P. Pullumbi, and F. X. Coudert, *ELATE: an open-source online application for analysis and visualization of elastic tensors*, J. Phys.: Condens. Matter **28**, 275201 (2016).

[142] N. W. Ashcroft and N. D. Mermin, *Solid State Physics* (Holt-Saunders, Philadelphia, 1976).

[143] G. Grimvall, *Thermophysical Properties of Materials* (Elsevier, 1999).

[144] A. Jain, R. Pankajavalli, S. Anthonysamy, K. Ananthasivan, R. Babu, V. Ganesan, and G. S. Gupta, *Determination of the thermodynamic stability of $TiB_2$*, J. Alloys Compd. **491**, 747 – 752 (2010).

[145] M. W. Chase, Jr., *NIST-JANAF Thermochemical Tables* (American Chemical Society and American Institute of Physics for the National Institute of Standards and Technology, Woodbury, NY, 1998), 4th edn.

[146] J. W. Zimmermann, G. E. Hilmas, G. W. Fahrenholtz, R. B. Dinwiddie, W. D. Porter, and H. Wang, *Thermophysical Properties of ZrB2 and $ZrB_2$–SiC Ceramics*, J. Amer. Ceram. Soc. **91**, 1405–1411 (2008).

[147] E. F. Westrum and G. Feick, *Heat capacities of $HfB_{2.035}$ and $HfC_{0.968}$ from 5 to 350 K*, J. Chem. Thermodyn. **9**, 293 – 299 (1977).

[148] H. L. Schick, ed., *Thermodynamics of Certain Refractory Compounds* (Academic Press, New York, USA, 1966).

[149] R. Loehman, E. Corral, H. P. Dumm, P. Kotula, and R. Tandon, eds., *Ultra High Temperature Ceramics for Hypersonic Vehicle Applications* (SAND2006-2925, Albuquerque, USA, 2006).

[150] W. Lengauer, S. Binder, K. Aigner, P. Ettmayer, A. Guillou, J. Debuigne, and G. Groboth, *Solid state properties of group IVb carbonitrides*, J. Alloys Compd. **217**, 137 – 147 (1995).

[151] A. G. Turchanin and A. E. Polyakov, *Thermodynamic properties of hafnium carbide in 0-3000 K temperature interval*, Izv. Akad. Nauk SSSR, Neorg. Mater.; (USSR) **18:3**, 404–406 (1982).

[152] E. K. Storms, *The Refractory Carbides*, Refractory materials : a series of monographs (Academic Press, 1967).

[153] E. F. Westrum and J. A. Sommers, *Heat capacity of hafnium mononitride from temperatures of 5 to 350 K: An estimation procedure*, J. Therm. Anal. Calorim. **69**, 103 – 112 (2002).

[154] F. I. Ajami and R. K. MacCrone, *Thermal expansion, Debye temperature and Gruneisen constant of carbides and nitrides*, J. Less-Common Met. **38**, 101 – 110 (1974).

[155] M. A. Blanco, E. Francisco, and V. Luaña, *GIBBS: isothermal-isobaric thermodynamics of solids from energy curves using a quasi-harmonic Debye model*, Comput. Phys. Commun. **158**, 57–72 (2004).

[156] C. Toher, J. J. Plata, O. Levy, M. de Jong, M. D. Asta, M. Buongiorno Nardelli, and S. Curtarolo, *High-throughput computational screening of thermal conductivity, Debye temperature, and Grüneisen parameter using a quasiharmonic Debye model*, Phys. Rev. B **90**, 174107 (2014).

[157] D. E. Gray and A. A. Bennett, *American Institute of Physics Handbook*, McGraw-Hill handbooks (McGraw-Hill, 1972).

[158] A. C. Lawson, D. P. Butt, J. W. Richardson, and J. Li, *Thermal expansion and atomic vibrations of zirconium carbide to 1600 K*, Philos. Mag. **87**, 2507–2519 (2007).

[159] Y. S. Touloukian, R. W. Powell, C. Y. Ho, and P. G. Klemens, *Thermophysical Properties of Matter - the TPRC Data Series.* (IFI/Plenum, 1970-1979).

[160] K. Aigner, W. Lengauer, D. Rafaja, and P. Ettmayer, *Lattice parameters and thermal expansion of $Ti(C_xN_{1-x})$, $Zr(C_xN_{1-x})$, $Hf(C_xN_{1-x})$ and $TiN_{1-x}$ from 298 to 1473 K as investigated by high-temperature X-ray diffraction*, J. Alloys Compd. **215**, 121 – 126 (1994).

[161] V. S. Bogdanov, V. S. Neshpor, Y. D. Kondrashev, A. B. Goncharuk, and A. N. Pityulin, Sov. Powder. Metall. Metal. Ceram. **21**, 412 (1982).

[162] B. Lönnberg, *Thermal expansion studies on the group IV–VII transition metal diborides*, J. Less-Common Met. **141**, 145 – 156 (1988).

[163] W. A. Paxton, T. E. Özdemir, I. Şavklıyıldız, T. Whalen, H. Biçer, E. K. Akdoğan, Z. Zhong, and T. Tsakalakos, *Anisotropic Thermal Expansion of Zirconium Diboride: An Energy-Dispersive X-Ray Diffraction Study*, J. Ceram. **2016**, 8346563 (2016).